RESEARCH ARTICLE | APRIL 17 2023

The effects of pulsed blowing jets on power gain of vortex-induced vibrations of a circular cylinder ⊘

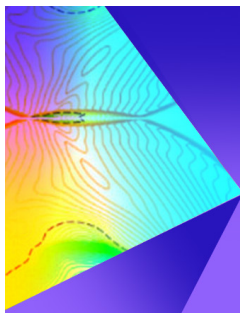Yujie Guo ; Zhengui Huang ✉ ; Chun Zheng ; Zhihua Chen ✉

Check for updates

View Online   Export Citation   CrossMark

Physics of Fluids

Special Topic: Shock Waves

Submit Today!

AIP Publishing

The effects of pulsed blowing jets on power gain of vortex-induced vibrations of a circular cylinder

Yujie Guo,[1] Zhengui Huang,[1,a] Chun Zheng,[2] and Zhihua Chen[1,a]

AFFILIATIONS

[1]National Key Laboratory of Transient Physics, Nanjing University of Science and Technology, Nanjing 210094, China
[2]School of Mechanical Engineering, Nanjing University of Science and Technology, Nanjing 210094, China

[a]Authors to whom correspondence should be addressed: hzgkeylab@njust.edu.cn and chenzh@njust.edu.cn

ABSTRACT

To enhance the power gain of vortex-induced vibration of a circular cylinder, the active control method of pulsed blowing jets located at $\theta = 90°$ is utilized to intensify its oscillation with the two-dimensional simulation of Reynolds-averaged Navier–Stokes at $2.0 \times 10^4 \leq Re \leq 9.6 \times 10^4$. Different from traditional continuous jets, the blowing jets used in this paper start once the cylinder moves to the upper limited position and last for a certain duration. Based on the combination of nine momentum coefficients and four pulse durations of the jets, the oscillation responses of the cylinder at a series of reduced velocities are calculated and distinct responses are observed in three branches. In the initial branch ($U^* \leq 4.27$), no matter what the values of C_μ and n are, the vortex patterns keep 2S accompanied by the amplitude ratios vibrating around the benchmarks. In the fore part of the upper branch ($4.27 < U^* \leq 6.17$), as $C_\mu \leq 0.1005$, the control effect is similar to that at $U^* \leq 4.27$; as $C_\mu > 0.1005$, both slight enhancement and suppression in amplitude ratios are observed, as well as the small values of power gain ratios. In the rear part of the upper branch and lower branch ($U^* > 6.17$), the enlarged disturbance of the jets to wake results in enhanced amplitude ratios for most cases. Galloping is observed at $n = 1/4$ and $1/2$ with a maximum amplitude ratio 13 times the benchmark, except for some suppressed cases at $C_\mu > 0.1005$, $n = 1/16$, and $1/8$. Though large amplitude ratios are achieved, considering more energy consumed as C_μ increases, the better control strategy with η ranging from 5.45% to 19.78% falls in $U^* > 6.17$ and $C_\mu < 0.1005$.

I. INTRODUCTION

Over the past decades, greatly increased requirements for energy lead to a sharp reduction in reserves of traditional fossil fuels and phase-out plans for coal-fired plants have been pronounced by European countries.[1] Thus, numerous scholars have devoted to exploiting clean and renewable energy to support sustainable development of human society.[2] Among all the renewable energy sources, marine hydrokinetic energy (MHK) is quite popular due to the abundant reserves in the oceans, which cover more than 70% of the earth's surface,[3,4] and flow-induced vibrations (FIVs) have become research hotspots. Vortex-induced vibrations (VIVs) and galloping are common phenomena of FIVs[5] in water. VIVs are resonant types of responses that are relevant with the inflow velocity and characteristics of the structure. High amplitudes in a broad range of velocity are observed when the shedding frequency is at or near the natural frequency of a circular cylinder.[6] However, the non-circular cylinders with sharp corners are more susceptible to galloping that occurs as the cylinder is dynamically unstable[7] and results in significant large-amplitude and low-frequency oscillations.[8]

Based on the characteristics of VIVs and galloping, lots of hydrodynamic energy converters are invented. Through comprehensive consideration of high energy density, low maintenance, being friendly to marine life, a proper life cycle, and being robust, Bernitsas *et al.*[9] proposed a novel bladeless device named VIVACE, which can extract kinetic energy from VIVs by a circular cylinder over a quite broad range, even at low velocities. Another innovative system with the hydraulic turbine placed on the coast is invented by Barbarelli *et al.*[10] to reduce the construction costs, nevertheless, at the expense of lower efficiencies. Harvesting energy from the tidal current is implemented by a submerged blade, which is connected to the device on coast through a four-bar linkage. Zhu *et al.*[11] invented an energy converter consisting of a circular cylinder and free-to-rotate pentagram impeller in TrSL2 and TrSL3 regimes and found that the hydrodynamic instability of the system is enhanced due to the presence and rotation of the impeller, which is beneficial for energy extraction. More different configurations of hydrodynamic energy harvesters based on VIVs and galloping can be seen in the review.[12]

No matter what types of the above-mentioned energy harvesters are, the energy source lies in the interaction between the oscillators and water, namely, strong coupling in fluid–structure interaction (FSI).[13] Therefore, a feasible way to improve the performance of the energy harvesters is to enhance the oscillation of the oscillator. Modifications in geometrical shapes of the cross sections have been widely used. Inspired by the large surface curvature of fish tails, Shi et al.[14] analyzed the hydrodynamic responses of an elliptic cylinder with different aspect ratios and found that a decrease in the cylinder's short diameter strengthened the shedding vortices, lift forces, amplitudes, and ultimately output voltage. After comparison of the FIV responses of the cylinders with different cross sections (PTC-cylinder, square, Q-trapezoid I, and triangular), Ding et al.[15] found that the oscillations of PTC-cylinder and Q-trapezoid I were stronger than other cylinders, and the optimum regime for energy harvesting is the VIV upper branch, though high amplitude is observed in the galloping branch. To combine the advantages of VIVs and galloping, Wang et al.[16] proposed an innovative energy scavenger with three different cross-sectioned bluff bodies (a 3/4 cylinder and 1/4 cuboid; a 1/2 cylinder and 1/2 cuboid; and a 1/4 cylinder and 3/4 cuboid). The results show that only appropriate combinations of the cross sections and attack angles could enhance the maximum voltage output. Except for the large transformation of the cross section profile, small modifications on the surface of the bluff body can also result in the enhancement of energy harvesting. The effects of convex[17] and etched concave[18] metasurfaces of an ordinary circular cylinder on its aerodynamic characteristics are investigated by Wang et al. Among all different metasurfaces, the convex hemisphere, convex tri-prism, and the concave hourglass patterns are beneficial for enhancing VIVs with enlarged lock-in regions; in contrast, other patterns suppress the VIVs or are not inappropriate. Passive turbulence control (PTC), another method with roughness strips attached on the cylinder's surface, is investigated by the team of Bernitsas[19–22] to realize the purpose of transiting VIV to galloping.

In addition to the geometrical modifications of bluff bodies, wake-induced vibration (WIV) that sets the oscillator at the wake of another upstream cylinder (free or fixed) to enhance the instability also plays an important role in improving energy harnessing. Tamimi et al. carried out a series of research works on WIV, which mainly focused on the different tandem configures of the oscillators (circular–square,[23] circular–circular, square–circular, diamond–circular,[24] square–square, and diamond–diamond[25]) motion states of the upstream cylinder (fixed or free),[26] and spacing ratios between the tandem cylinders. Considering the harvesting capabilities, when the upstream cylinder is fixed (square–square and diamond–diamond), the performance of the tandem arrangements is better than that of the single cylinder both in mechanical power and maximum efficiency, and the diamond oscillators are superior to the square ones;[25] when coupled with an electromagnetic transducer, the maximum total efficiency of the double oscillator devices with an upstream free cylinder is improved by 97% at the optimum electromagnetic transduction factor.[26] Tang et al.[27] numerically studied the effects of spacing and radius ratios on the hydrodynamic responses of the downstream cylinder in-series arrangements. The results show that both the transition from VIV to galloping and suppression are observed for the square–cylinder system, and the optimal spacing and radius ratios are found out to enhance conversion efficiency. More similar literature works about the combination of geometrical modification and WIV are researched by Tang et al.,[28] Ding et al.,[29] Zhang et al.,[30] and Ding et al.[31]

As mentioned above, to enhance the performance of energy harvesters, numerous passive control strategies are researched in depth, whereas the active control, as well as an important flow control method with the advantages of controllability and maneuverability, such as suction/blowing, synthetic jet, electromagnetic forcing, and rotation, is usually utilized to suppress the destructive consequences of FIVs[32,33] rather than to enhance oscillation challengingly. Among all the active methods, suction/blowing has been widely used and suction is more effective in suppressing oscillations,[34] especially set near the separation points.[35] In the perspective of energy savings, the pulsed jets are superior to continuous jets[36] with similar performance in flow control. Only one related paper about active control for enhancing VIV has been searched yet. Based on an artificial neural network (ANN) trained by deep reinforcement learning (DRL), Mei et al.[37] gained effective suction/blowing strategy to enhance the energy output by 357.63% at a relatively small Re = 100. Therefore, it is necessary to analyze the effects of active control on energy harvesting enhancement to provide a reference for practical engineering.

In this paper, the effects of pulsed jets are analyzed on energy harnessing at $2.0 \times 10^4 \leq Re \leq 9.6 \times 10^4$ in the TrSL3 regime with a high lift.[38] In contrast to the remarkable suppression of suction, blowing is selected here. A single micro-orifice set on the top side of the cylinder (90°) aims to break up the structural symmetry to reach a high amplitude. The pulsed blowing with a combination of nine momentum coefficients (C_μ = 0.0016, 0.0063, 0.0251, 0.0565, 0.1005, 0.1570, 0.2261, 0.3077, and 0.4019) and four pulse durations (n = 1/16, 1/8, 1/4, and 1/2) supersedes the traditional continuous jet and starts when the cylinder moves to the upper limited position. The impacts on near wake structures, hydrodynamic coefficients, amplitude ratios, frequency ratios, and power gain ratios are discussed in detail to obtain optimal control parameters to enhance the oscillation and energy harnessing. The numerical methodology, such as fluid governing equations, jet model, validation of mesh, and computational domain, is present in Sec. II. The results and discussions are in Sec. III. Section IV presents the conclusions and prospects for future work.

II. NUMERICAL METHODOLOGY

Based on the previous literature works about bladeless energy converters, the schematic diagram of the oscillation system is simplified as a single degree of freedom (1DOF) spring-damping-mass system with an elastically mounted rigid circular cylinder moving in the vertical direction[39] as depicted in Fig. 1(a). The origin of the coordinate is set at the center of the circular cylinder, and the axis of x is consistent with the direction of the free incoming flow that is vertical to the axis of y in Fig. 1(b). The pulsed blowing jets are ejected from a micro-orifice with the width of $w_{width} = \pi D / 1000$ positioned at $\theta = 90°$ on the cylinder surface.

A. Fluid governing equations

The flow field around the circular cylinder in water can be considered to be incompressible and unsteady at the interested velocity of 0.25–1.2 m/s. The Reynolds-averaged Navier–Stokes (RANS) method that decomposed the solution parameters into time-averaged and
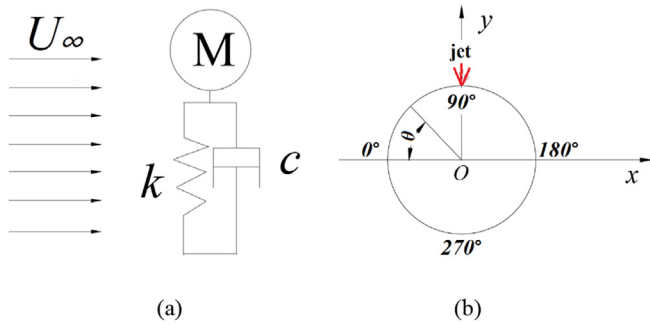
FIG. 1. Schematic diagram of the oscillating system: (a) schematic diagram of the system and (b) azimuthal angles.

fluctuating components[40] is used to calculate the fluid field around the cylinder. The fluid dynamics equations can be written as

$$\frac{\partial \bar{u}_i}{\partial x_i} = 0, \tag{1}$$

$$\frac{\partial \bar{u}_i}{\partial t} + \bar{u}_j \frac{\partial \bar{u}_i}{\partial x_j} = -\frac{1}{\rho}\frac{\partial \bar{p}}{\partial x_i} + \frac{\partial}{\partial x_j}\left(2 \upsilon S_{ij} - \overline{u_i' u_j'}\right), \tag{2}$$

$$\bar{S}_{ij} = \frac{1}{2}\left(\frac{\partial \bar{u}_i}{\partial x_j} + \frac{\partial \bar{u}_j}{\partial x_i}\right), \tag{3}$$

$$\tau_{ij} = -\rho \overline{u_i' u_j'} = 2\mu_t \bar{S}_{ij} - \frac{2}{3}\rho k \delta_{ij}, \tag{4}$$

where $\bar{u}_i$ and $\bar{p}$ are the mean velocity and pressure, respectively. ρ, υ, μ_t, k, $\bar{S}_{ij}$, τ_{ij}, and δ_{ij}, are the fluid density, molecular kinetic viscosity, turbulent eddy viscosity, turbulent kinetic energy, mean strain rate tensor, Reynolds stress tensor, and Kronecker delta function, respectively.

To enclose the fluid dynamics governing equations [Eqs. (1)–(4)], the Reynolds stress tensor is modeled using the shear stress transport (SST) k–ω turbulence model developed by Menter[41] which can be expressed as

$$\frac{D(\rho k)}{Dt} = \tau_{ij}\frac{\partial u_i}{\partial x_j} - \beta^* \rho \omega k + \frac{\partial}{\partial x_j}\left[(\mu + \sigma_k \mu_t)\frac{\partial k}{\partial x_j}\right], \tag{5}$$

$$\frac{D(\rho \omega)}{Dt} = \frac{\gamma}{\upsilon_t}\tau_{ij}\frac{\partial u_i}{\partial x_j} - \beta \rho \omega^2 + \frac{\partial}{\partial x_j}\left[(\mu + \sigma_\omega \mu_t)\frac{\partial \omega}{\partial x_j}\right]$$
$$+ 2(1 - F_1)\rho \sigma_{\omega 2}\frac{\partial k}{\partial x_j}\frac{\partial \omega}{\partial x_j}. \tag{6}$$

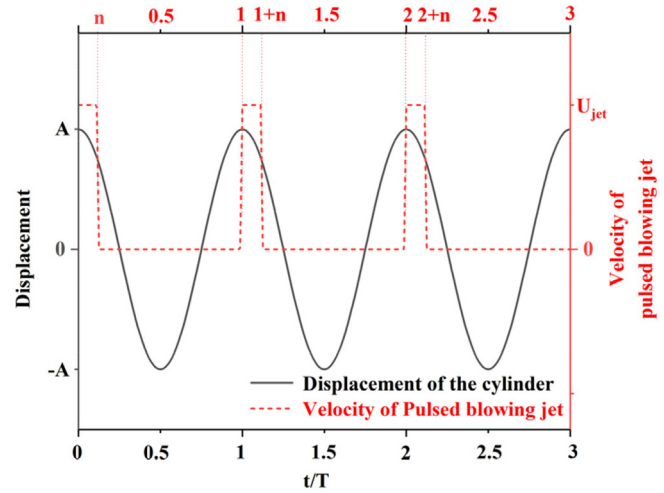More detailed description of Eqs. (5) and (6) can be referred in previous literature.[41]

FIG. 2. Pulsed blowing jet model.

To solve the governing equations, the FVM (finite volume method) and the algorithm of SIMPLE (Semi-implicit method for pressure-linked equations) are employed.

B. Pulsed blowing jet model

The schematic of the blowing jet model is shown in Fig. 2. The horizontal axis t/T represents the ratio of the real time (t) to oscillation cycle of the smooth cylinder (T). The solid black line indicates the displacements of the circular cylinder that is monitored in real time, and the red dotted line indicates the mean velocity of the pulsed blowing jet. It can be seen that the pulsed blowing jet is activated once the cylinder reaches its upper limit position. The duration (nT) and the velocity (U_{jet}) of the jet that are both critical parameters are controlled in the UDF code according to different cases. To analyze the effects of duration of blowing jet, the values of n are taken to be 1/2, 1/4, 1/8, and 1/16 in this paper. To compare the momentum flux of the pulsed blowing jets with the free stream, the momentum coefficient C_μ[42] is introduced as

$$C_\mu = \frac{2 U_{jet}^2 d}{U_\infty^2 D}, \tag{7}$$

where U_{jet}, U_∞, d, and D are the mean velocity of the jet, velocity of free stream, the width of the micro-orifice, and the diameter of the cylinder, respectively. The concerned durations (n) and momentum coefficients (C_μ) of the pulsed blowing jets are listed in Table I.

TABLE I. Durations and momentum coefficients.

n					C_μ				
1/2	0.0016	0.0063	0.0251	0.0565	0.1005	0.1570	0.2261	0.3077	0.4019
1/4	0.0016	0.0063	0.0251	0.0565	0.1005	0.1570	0.2261	0.3077	0.4019
1/8	0.0016	0.0063	0.0251	0.0565	0.1005	0.1570	0.2261	0.3077	0.4019
1/16	0.0016	0.0063	0.0251	0.0565	0.1005	0.1570	0.2261	0.3077	0.4019

C. Structural oscillation equation

The motion of the cylinder is described by the oscillation equation,

$$M\ddot{y}_t + c\dot{y}_t + ky_t = F_{fluid,y,t} + F_{jet}, \tag{8}$$

where M, y, c, and k are the total mass, displacement, damping coefficient, and spring stiffness, respectively. Two forces exerted on the cylinder are in the right-hand side of the equation: $F_{fluid,y,t}$ and F_{jet}. $F_{fluid,y,t}$ that can be solved in the CFD solver is the component of hydrodynamic force in the y direction. According to Newton's second law, F_{jet} that is the mean force in the duration of nT can be expressed as

$$F_{jet} = \frac{d}{dt}(mv) = \frac{\rho \cdot nT \cdot U_{jet} \cdot A_{jet} \cdot U_{jet}}{nT} = \rho U_{jet}^2 A_{jet}, \tag{9}$$

where A_{jet} is the area of the orifice that can be considered as a spanwise slot with a unit length along the cylinder in this two-dimensional model.

To solve the second-order linear ordinary differential equation [Eq. (8)], a step by step integration method called Newmark β is used. Based on the hypothesis of linear acceleration, the original equation is discretized into a series of equations at different moments. For example, the displacement and velocity at time $t + \Delta t$ could be written as

$$y_{t+\Delta t} = y_t + \dot{y}_t\Delta t + \left(\frac{1}{2} - \beta\right)\ddot{y}_t\Delta t^2 + \beta\ddot{y}_{t+\Delta t}\Delta t^2, \tag{10}$$

$$\dot{y}_{t+\Delta t} = \dot{y}_t + [(1-\gamma)\ddot{y}_t + \gamma\ddot{y}_{t+\Delta t}]\Delta t, \tag{11}$$

where $y_{t+\Delta t}$, $\dot{y}_{t+\Delta t}$, $\ddot{y}_{t+\Delta t}$, y_t, $\dot{y}_t$, and $\ddot{y}_t$ are the displacement, velocity, and acceleration at time $t + \Delta t$ and t, respectively. γ and β are constants that make the method unconditionally stable with $\gamma = 0.5$ and $\beta = 0.25$.[8] The motion equation of the cylinder at time $t + \Delta t$ is

$$M \cdot \ddot{y}_{t+\Delta t} + c \cdot \dot{y}_{t+\Delta t} + K \cdot y_{t+\Delta t} = F_{fluid,y,t+\Delta t} + F_{jet,t+\Delta t}. \tag{12}$$

Combining Eq. (10) with Eq. (11), Eq. (12) can be reorganized as

$$\bar{K} \cdot y_{t+\Delta t} = \bar{F}, \tag{13}$$

$$\bar{K} = K + \frac{1}{\beta\Delta t^2} \cdot M + \frac{\gamma}{\beta\Delta t} \cdot c, \tag{14}$$

$$\begin{aligned}\bar{F} = F_{fluid,y,t+\Delta t} + F_{jet,t+\Delta t} \\ + \left[\frac{1}{\beta\Delta t^2} \cdot y_t + \frac{1}{\beta\Delta t} \cdot \dot{y}_t + \left(\frac{1}{2\beta} - 1\right) \cdot \ddot{y}_t\right] \cdot M \\ + \left[\frac{\gamma}{\beta\Delta t} \cdot y_t + \left(\frac{\gamma}{\beta} - 1\right) \cdot \dot{y}_t + \left(\frac{\gamma}{2\beta} - 1\right) \cdot \Delta t \cdot \ddot{y}_t\right] \cdot c.\end{aligned} \tag{15}$$

Then, the calculation process of displacement, velocity, and acceleration at time $t + \Delta t$ is fulfilled by the UDF embedded in the fluid solver according to the Eqs. (9)–(15).

D. Mesh and computational domain independence check

As depicted in Fig. 3, the computational domain is a rectangle that is divided into three parts: I, II, and III. The length of the rectangle in the x direction is chosen to be 40D, which is large enough for the VIV with 1DOF.[43] However, considering the potential large
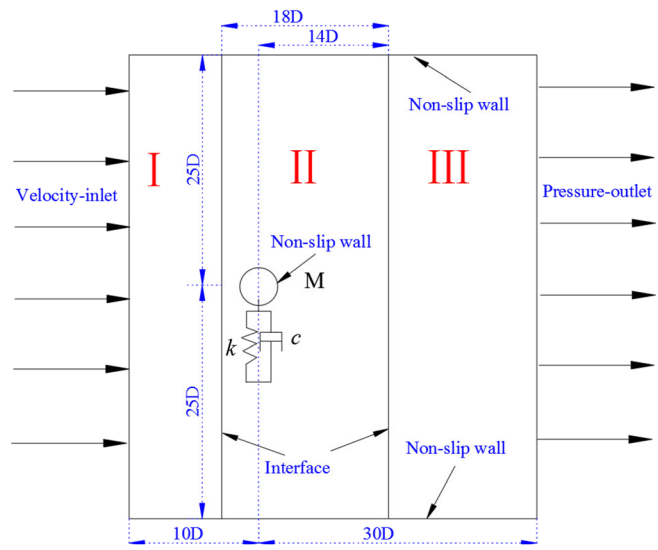

FIG. 3. Computational domain.

displacements in the transverse direction when the pulsed blowing jets are activated, the width of the rectangle in the y direction should be large enough to diminish the effects of boundaries on the flow field.[15] Three values of the width are taken to be 40D, 50D, and 60D with the blockage ratios 2.5%, 2%, and 1.7%, respectively. Based on trial calculations, the amplitude response of the cylinder is higher than other cases when $n = 0.5$, $C_\mu = 0.4019$ at $U_\infty = 1.15$ m/s. Hence, this case is used to check the independence of computational domain. The relative errors of amplitude ratios based on case 3 are listed in Table II, and the error between cases 2 and 3 is smaller. Thus, the width larger than 50D has little effect on the results, and case 2 is selected, as illustrated in Fig. 3. In addition, there are four kinds of boundary conditions for the computational domain: velocity-inlet, pressure-outlet, non-slip wall, and interface.

For the oscillation with large displacements, the traditional dynamic mesh technology may lead to negative volumes and calculation termination. Therefore, a new method for moving meshes is chosen. Meshes in part II can move with the rigid cylinder accompanied by the deformation of the upper and down boundaries to absorb the movements.[40,44] The boundaries between I and II and II and III are both interfaces through which interpolation operation is allowed. To better capture the flow characteristics close to the cylinder, a circular topology layout within 2D-diameter domain consistent with the flow direction is set. The mesh size of the first layer around the cylinder

TABLE II. Independence check of computational domain ($U_\infty = 1.15$ m/s, $n = 0.5$, and $C_\mu = 0.4019$).

	Width	Number of meshes	A/D	Relative error
Case 1	40D	97 476	3.2985	−0.18%
Case 2	50D	115 356	3.3056	0.03%
Case 3	60D	133 236	3.3046	· · ·

TABLE III. Independence check of meshes ($U_\infty = 0.7$ m/s, smooth cylinder).

	Central circle: circumferential × radial	Number of meshes in Part II	A/D	Relative error
Coarse	220 × 45	71 000	1.0541	1.13%
Medium	260 × 70	100 860	1.0434	0.11%
Fine	340 × 100	125 900	1.0423	—

should be small enough to satisfy the demand of SST k–ω turbulent model for $y^+ < 1$ and 1.2×10^{-5} m is selected. The meshes are denser near the wall and then increase gradually at the rate of 1.05. In other parts, the mesh topology is rectangular and becomes sparser away from the cylinder. Three grid densities with different numbers of nodes in the circumferential and radial direction of the 2D-diameter circle around the cylinder are given in Table III. The amplitude response of smooth cylinder at $U_\infty = 0.7$ m/s is used to assess the meshes. The results indicate that the case larger than 100 860 cells in part II has little effect on the relative error, which is calculated based on the fine density. For the sake of accuracy and efficiency, the medium density is selected. The meshes in the whole computational domain and close-up near the cylinder wall are shown in Figs. 4(a) and 4(b). All the values of y^+ on the cylinder during calculation that are carefully checked meet the requirements, and the two representative histories at different moments are given in Fig. 4(c).

E. Numerical method validation

To validate the accuracy of this numerical method, the response of smooth cylinder is simulated in the range of 0.25–1.2 m/s ($Re = 2.0 \times 10^4$–9.6×10^4) in this paper. The range of velocities falls in the regime of TrSL3, which means that the shear layer is fully saturated contributing to a relatively high lift.[15,38] The steps to obtain oscillation responses of the cylinder are as follows: First, the hydrodynamic forces exerted on the cylinder are calculated by solving the governing equations; second, based on the forces achieved in the last step, the motion equations of the cylinder are solved by the UDF code embedded in CFD solver to get the displacement, velocity, and acceleration in the next state; and finally, the meshes are modified based on the new position of the cylinder to prepare for the calculation of hydrodynamic forces in next time step. The essential parameters of the oscillation system[45] are listed in Table IV. The reduced velocity U^* introduced to describe the variation of amplitudes is defined as

$$U^* = \frac{U_\infty}{f_{n,water} D}. \tag{16}$$

The histories of amplitude and frequency ratios vs reduced velocity are shown in Fig. 5. Compared with the previous experimental[46] and numerical[45] results, it can be seen that the amplitude ratios in Fig. 5(a) could be divided into three branches: initial branch ($2.37 < U^* \leq 4.27$), upper branch ($4.27 < U^* < 7.12$), and lower branch ($7.12 \leq U^* < 11.38$). The amplitude ratios increase first to a high value and then decrease with the reduced velocity. The ranges of the reduced velocity for the three branches are consistent with previous data. As shown in Fig. 5(b), the growth trend of frequency ratios with the

reduced velocity is also similar. Thus, the main features of oscillation could be obtained by the numerical method. It can be assumed that the accuracy of the results in this paper is acceptable though some deviations occur.

III. RESULTS AND DISCUSSION

To analyze the effects of the pulsed blowing jets on the power gain of the cylinder, the oscillation responses are calculated at the selected reduced velocities of 4.27, 5.22, 6.17, 7.12, 8.07, 9.01, 9.96, and 10.91, which are distributed in the initial, upper, and lower branch, respectively. The influences of momentum coefficients (C_μ) and durations (n), as two main parameters of the jets, on amplitude ratios, frequency ratios, near wake structures, hydrodynamic coefficients, and power gain ratios are discussed in this part.

A. Effects on the near wake structures and hydrodynamic coefficients

To explain the physical mechanisms of the pulsed blowing jets' influences on the oscillation in a visualized method, comparisons of the representative near wake structures between the cylinder with and without control in three branches ($U^* = 4.27$, 6.17, and 10.91) are discussed here. The wake structures of the cases at different C_μ ($C_\mu = 0.0016$, 0.1005, and 0.4019) for the same n ($n = 1/2$) and at different n ($n = 1/4$, 1/8, and 1/16) for the same C_μ ($C_\mu = 0.4019$) are shown in Figs. 6 and 8, respectively. In addition, lift coefficient (C_y), as another important factor of the 1DOF system in the transverse direction, is introduced to describe the lift exerted on the cylinder in the y direction,

$$C_y = \frac{F_{fluid,y}}{\frac{1}{2}\rho U_\infty^2 D}. \tag{17}$$

The histories of non-dimensional C_y/C_{y0} (C_{y0}, the maximum lift coefficient for the smooth cylinder) and displacements vs t/T are given in Figs. 7 and 9, where T_1, T_2, and T_3 are the vibration cycles of the smooth cylinder at $U^* = 4.27$, 6.17, and 10.91, respectively. As depicted in the first line of Fig. 6, 2S, 2P$_0$, and 2P modes are observed for the smooth cylinder without control in the initial, upper, and lower branch, respectively. As a transition mode from 2S to 2P, 2P$_0$[47] has a much weaker secondary vortex, which decays rapidly in each pair, different from the typical 2P mode with two vortices of similar strength in each pair. The features of the wake agree well with the results in previous literature.[19]

(a) Compared with the cases without control, there are little changes in the wake at $U^* = 4.27$, no matter what the values of C_μ are as shown in the first column of Fig. 6. At $C_\mu = 0.0016$, the faint vortex induced by the jet is trapped within the shedding vortex in the shear layer and dissipates immediately once the jet is off with little disturbance injected to the flow field. The fluctuations of the lift coefficient are also quite small at the moments when jet is on and off for $C_\mu = 0.0016$ as shown in Fig. 7(a). However, as C_μ increases, the jet rushes out of the shear layer to wrap up the vortices, which is about to shed leading to a delay of the shedding process. The delay becomes more apparent for a larger C_μ with less peaks of lift coefficients (four peaks at $C_\mu = 0.0016$ and three peaks at $C_\mu = 0.4019$) in the same time, as shown in Fig. 7(a). In addition,
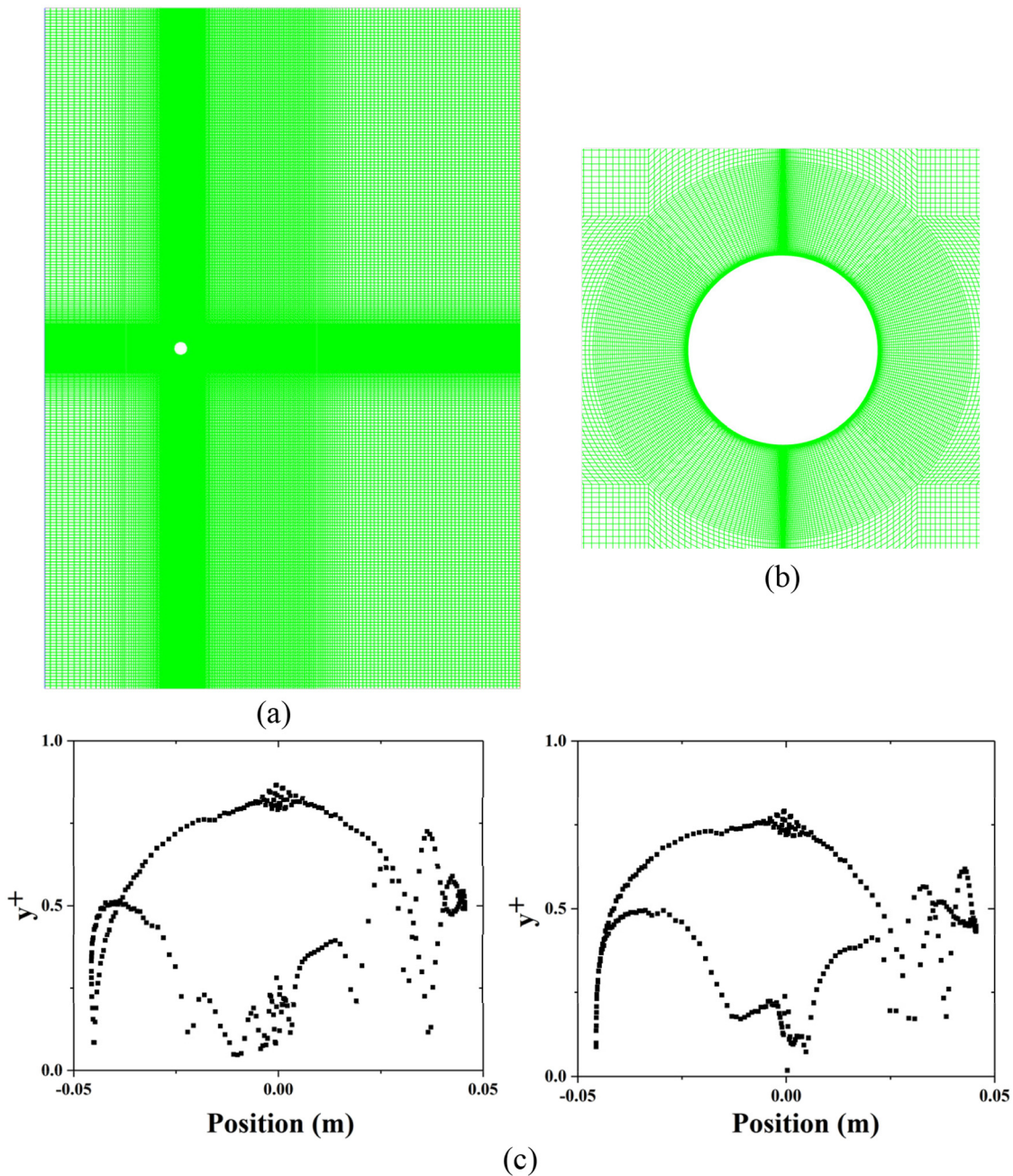
FIG. 4. Medium meshes: (a) entire computational meshes, (b) close-up of 2D-circle near the cylinder, and (c) y^+.

it can also be seen that the bigger C_μ is, the larger pressure fluctuations induced by the sudden injection and stop of the jets are. Despite these differences, for all controlled cases with different C_μ at $U^* = 4.27$ and $n = 1/2$, the vortex shedding patterns still keep 2S and the deviations of RMS (root mean square) of C_y/C_{y0} are within 10% compared with the benchmarks. What is more, the displacements vibrate around the

benchmark with a maximum difference of 20% as shown in the first figure of Fig. 7(d). Thus, C_μ is unable to greatly change the flow field and lifts on the cylinder at $n = 1/2$, as well as the displacements.

The comparisons of near wake structures and C_y/C_{y0} for different n at $U^* = 4.27$ and $C_\mu = 0.4019$ are illustrated in Figs. 8(a) and 9(a). It can be seen that all the vortex patterns

TABLE IV. Essential parameters.

Description	Symbol (unit)	Value
Length	L (m)	1.00
Diameter	D (m)	0.0912
Mass	M (kg)	13.63
Density of fluid	ρ (kg/m^3)	1000
Stiffness of spring	K (N/m)	1063
Damping coefficient	C (N·s/m)	30
Natural frequency	$f_{n,\text{water}}$ (Hz)	1.1556
Displaced mass of cylinder	M_d (kg)	6.5325
Mass ratio	$m^* = M/M_d$	1.725

keep 2S and the fluctuations of C_y/C_{y0} are almost equal at the same C_μ. Although there are differences in partial distribution of the C_y/C_{y0}, the deviations of RMS are still within 10%. Therefore, different pulse durations of the jets have little effects on the oscillation of the cylinder in the initial branch.

(b)   As depicted in the second column of Fig. 6, when $U^* = 6.17$ and $C_\mu = 0.0016$, the near wake structure is similar to the smooth cylinder. Due to little disturbance injected into the flow field with such small C_μ, both the lift coefficients and displacements basically coincide with the benchmarks in Figs. 7(b) and 7(d). However, different situations occur as C_μ increases. At $C_\mu = 0.1005$, 2T mode is observed with two more vortices shedding in one cycle. The vortex induced by the jet splits the vortex in the shear layer, and the amounts of shedding vortices raise. The slight increments in RMS of C_y/C_{y0} and amplitude are 15.2% and 3.8%, respectively. As C_μ increases to 0.4019, during the downward movement of the cylinder, the vortices induced by the jet become strong enough to shed itself and merge with the shedding vortices from the shear layer to form a stronger one, rather than just

wrap up or split the shedding vortices as aforementioned cases. T+P$_0$ mode with three more vortices shedding is observed during a half cycle of the oscillation. Both the amounts and strength of the vortices are elevated compared with the benchmarks. RMS of C_y/C_{y0} and amplitude ratios are raised by 87.4% and 31.7%, respectively. Hence, the oscillation of the cylinder is slightly enhanced as $C_\mu \geq 0.1005$ at $n = 1/2$.

The different effects of n are apparent at $U^* = 6.17$ and $C_\mu = 0.4019$ as shown in Figs. 8(b) and 9(b). The duration of the jet lasts for a quite short time at $n = 1/16$ and 1/8. The lengthened streamwise vortices about to shed, as well as the reduced transverse distance between vortices, lead to the decline in the amplitudes by -61.7% and RMS of C_y/C_{y0} by -62.3% at $n = 1/16$. As n increases, a longer duration will excite the shedding process with slight enhancement of oscillation at $n = 1/2$ as mentioned above.

(c)   Significant disturbances in the wake are observed at $U^* = 10.91$ as depicted in Fig. 6(c), even at small C_μ. When $C_\mu = 0.0016$, though the trapped vortices induced by the jet make the shedding pattern keep 2P, the transverse distance between the vortices is enlarged leading to the enhancements of amplitude and RMS of C_y/C_{y0} by 238.5% and 150.7%, respectively. When C_μ increases to 0.1005, the jet splits the vortices in the shear layer and P + 2T mode is observed with four additional shedding vortices in one cycle. As a result of the extra vortices, more frequent pressure changes around the cylinder can be seen from the fluctuations of C_y/C_{y0} in Fig. 7(c). The oscillation mode transits from VIV to galloping. As an example of typical galloping, the evolution of the vortex shedding in one cycle at $C_\mu = 0.4019$ with selected 12 positions is illustrated in Fig. 10. The jet is on and off at positions 1 and 7, respectively. The vortex induced by the jet rushes out the shear layer (position 1) and splits the negative vortices (positions 2 and 3). During the downward movement of the
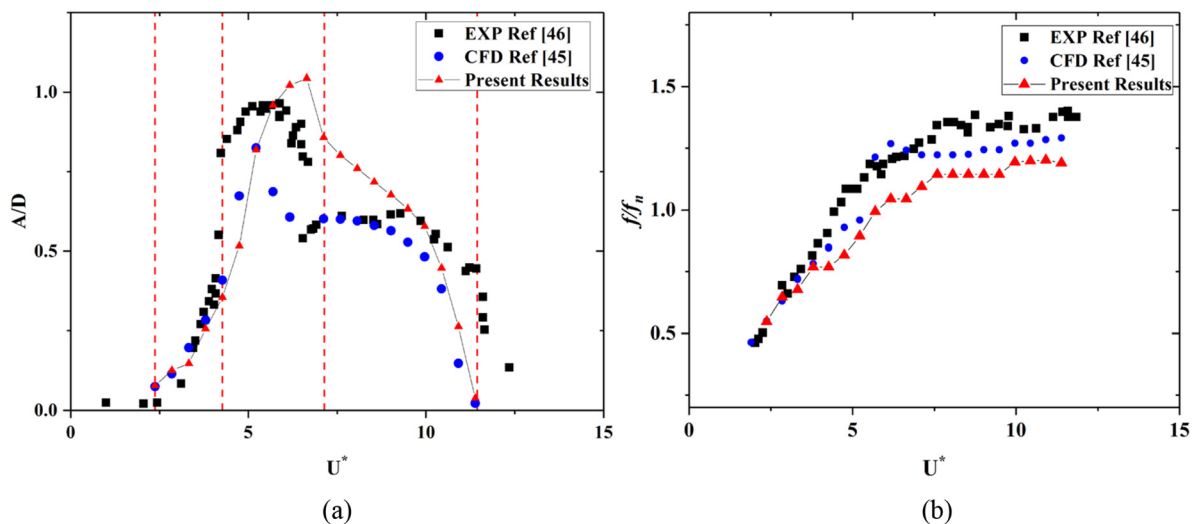

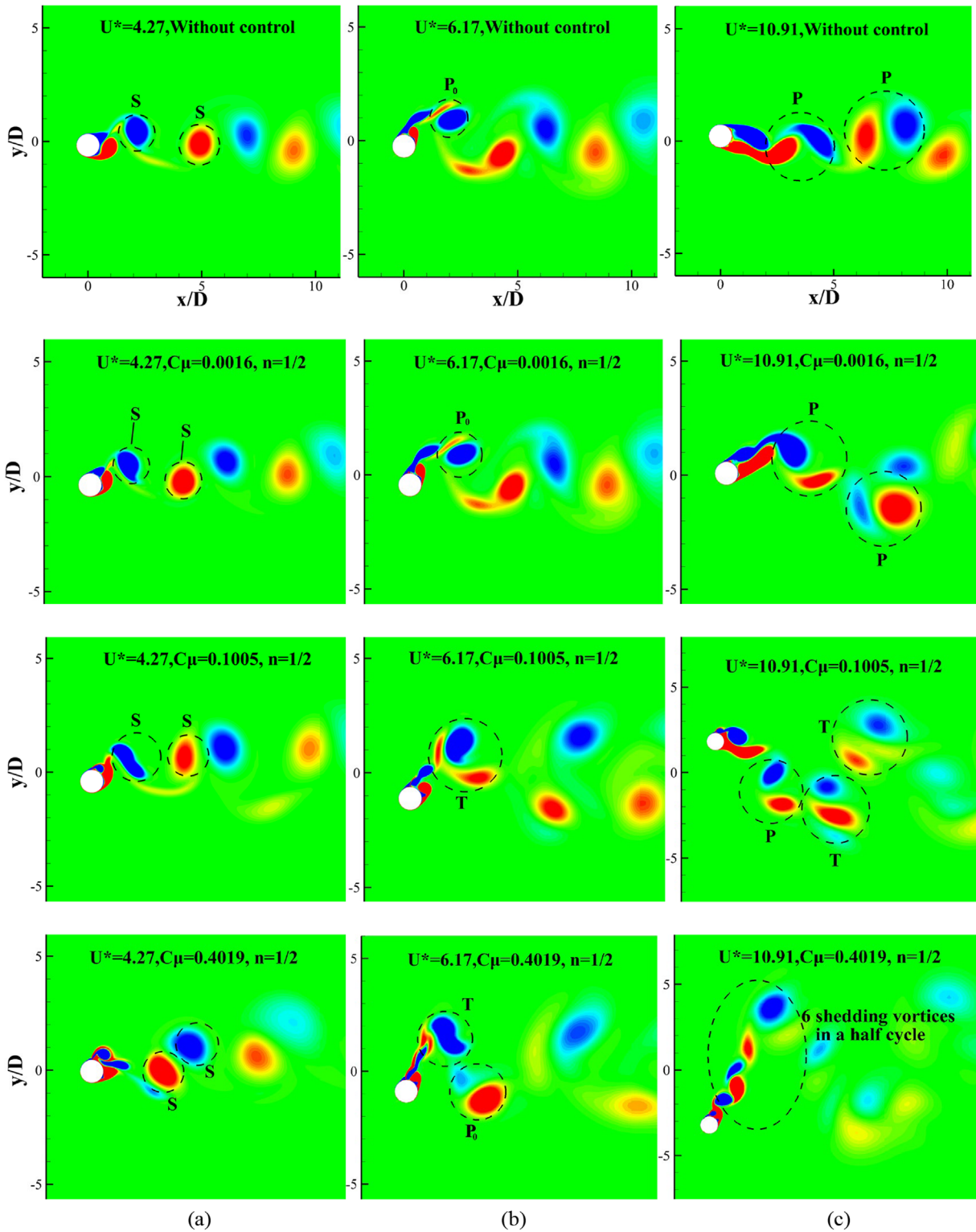**FIG. 5.** Comparison of (a) amplitude ratios and (b) frequency ratios between experimental and numerical results.

FIG. 6. Comparisons of near wake structures for different C_μ at $n = 1/2$: (a) initial branch ($U^* = 4.27$), (b) upper branch ($U^* = 6.17$), and (c) lower branch ($U^* = 10.91$).
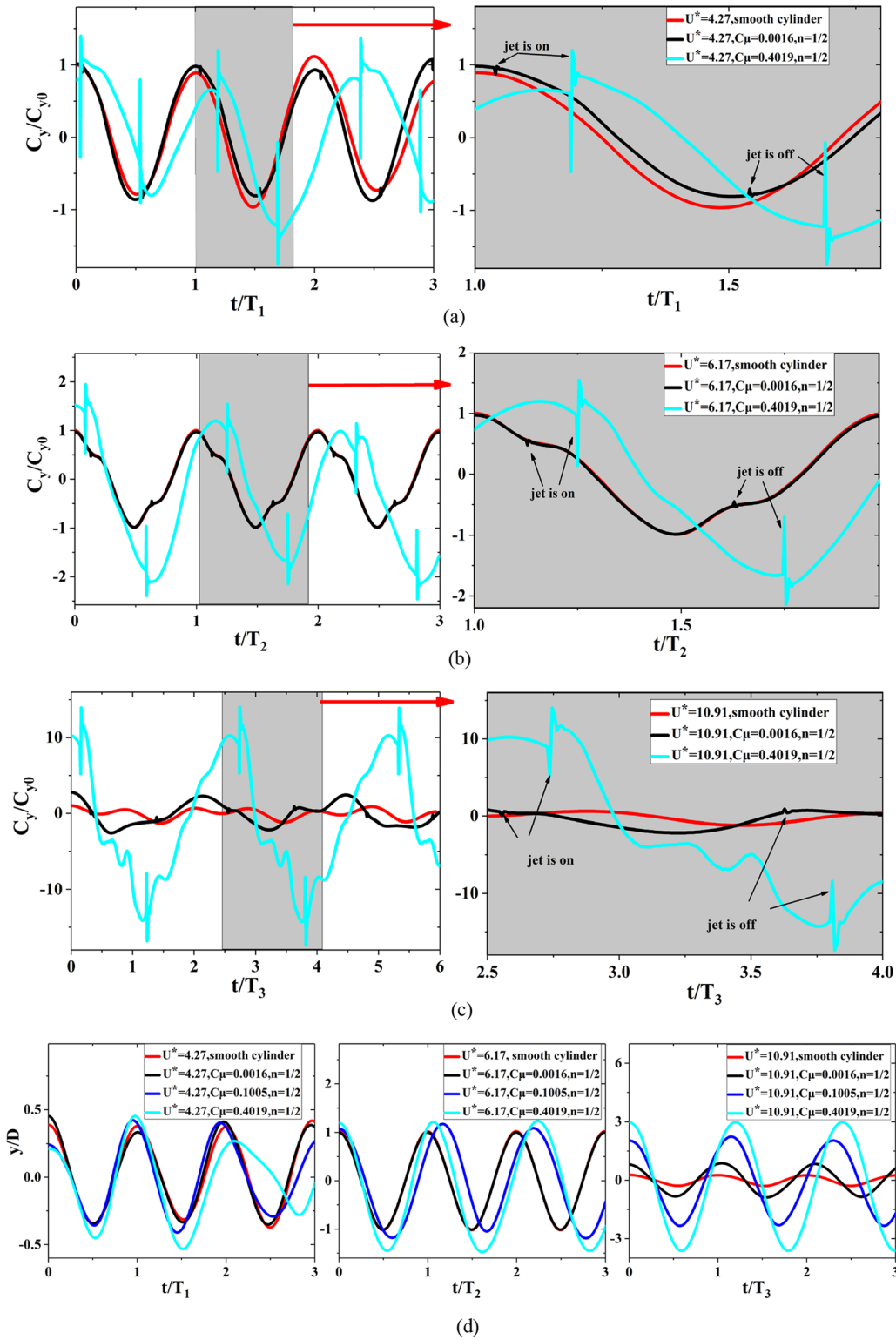
FIG. 7. Comparisons of C_y/C_{y0} and displacements for different C_μ at $n = 1/2$: (a) C_y/C_{y0} at $U^* = 4.27$, (b) C_y/C_{y0} at $U^* = 6.17$, (c) C_y/C_{y0} at $U^* = 10.91$, and (d) displacements at $U^* = 4.27$, 6.17, and 10.91.
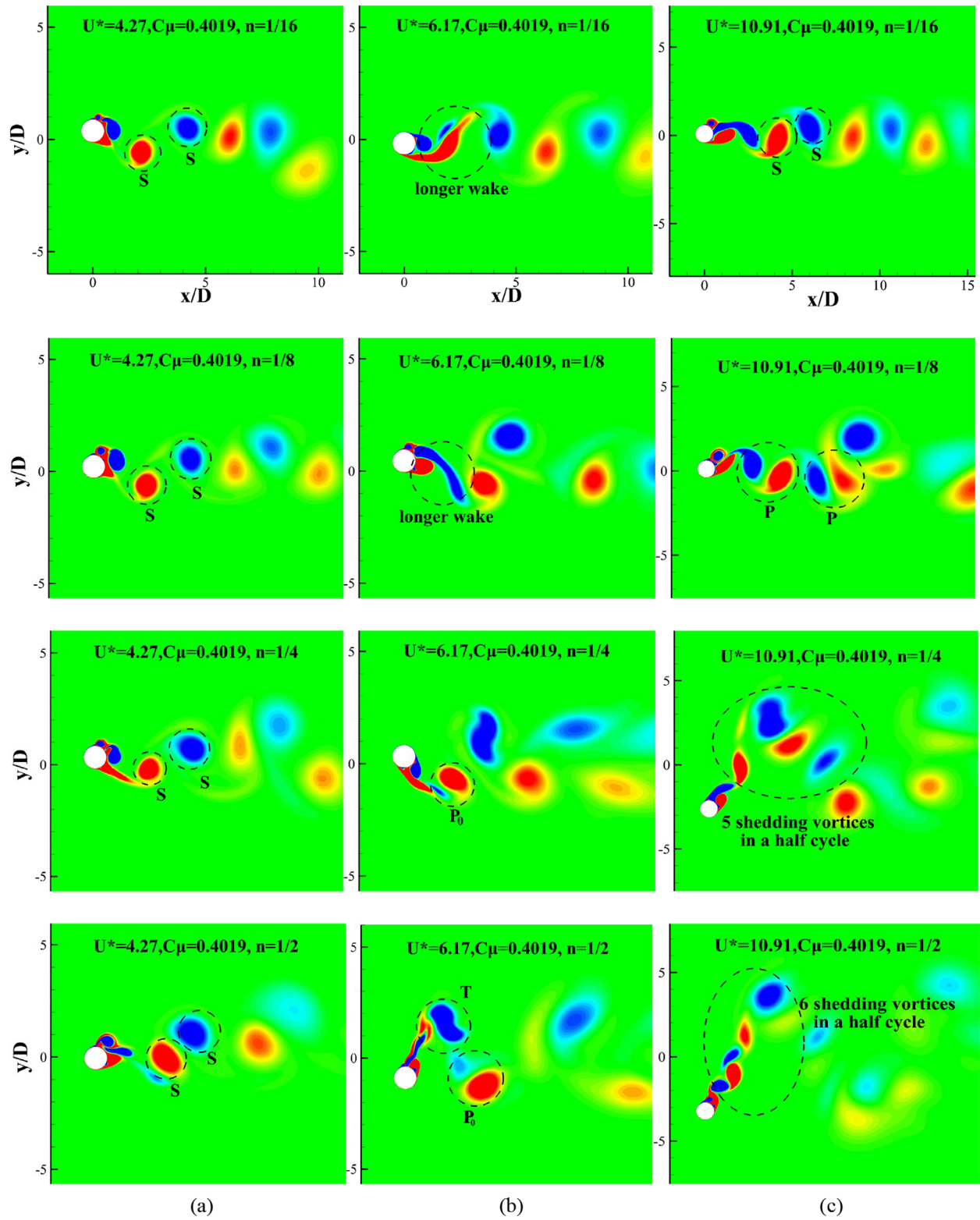
FIG. 8. Comparisons of near wake structures for different n at $C_\mu = 0.4019$: (a) initial branch ($U^* = 4.27$), (b) upper branch ($U^* = 6.17$), and (c) lower branch ($U^* = 10.91$).
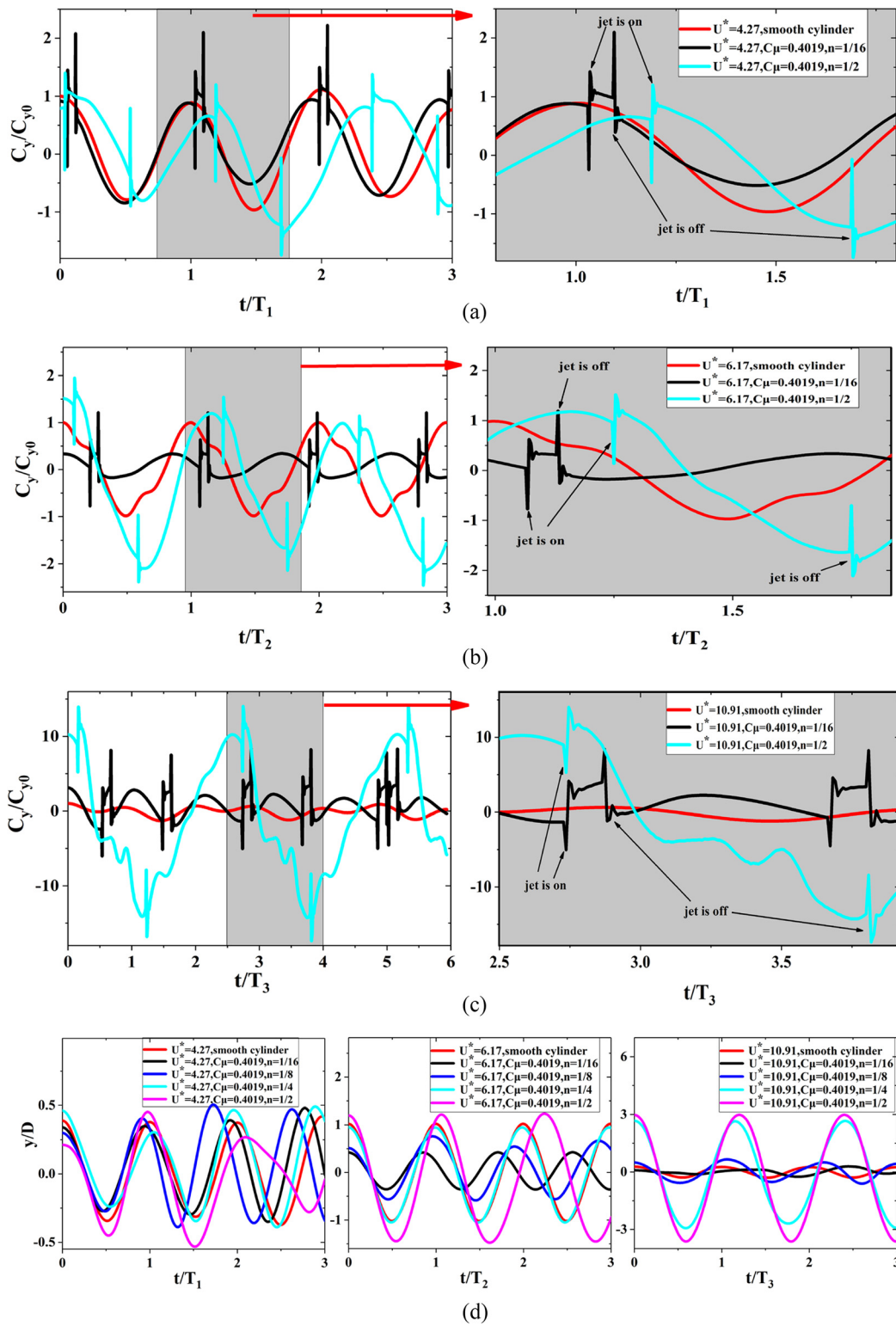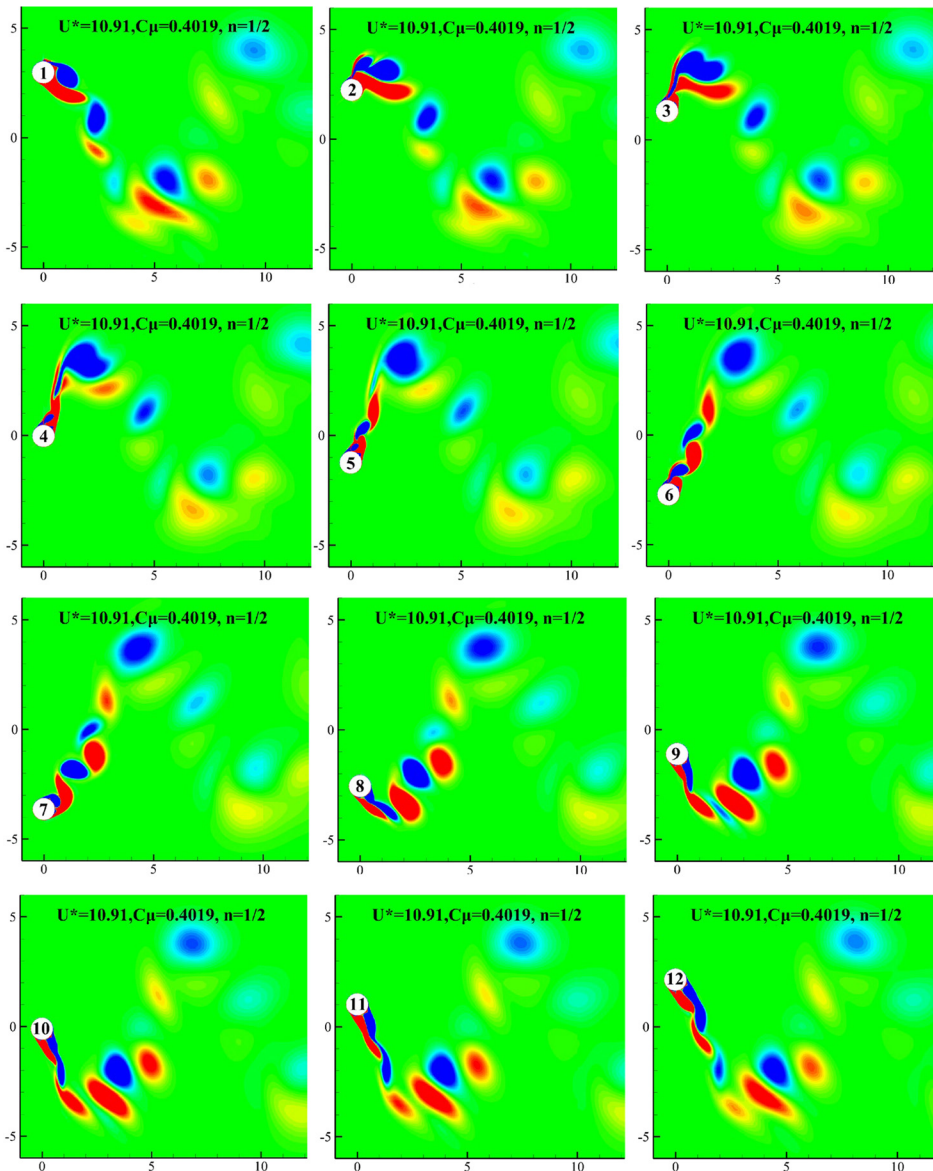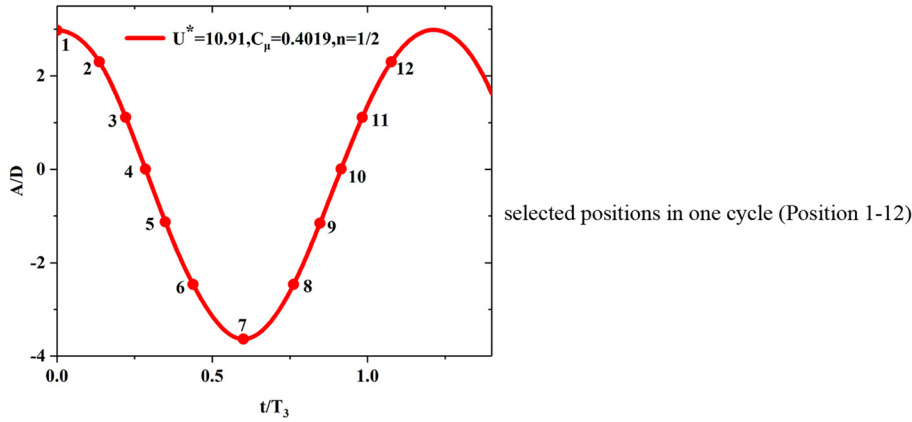
FIG. 9. Comparisons of C_y/C_{y0} and displacements for different n at $C_\mu = 0.4019$: (a) C_y/C_{y0} at $U^* = 4.27$, (b) C_y/C_{y0} at $U^* = 6.17$, (c) C_y/C_{y0} at $U^* = 10.91$, and (d) displacements at $U^* = 4.27$, 6.17, and 10.91.

FIG. 10. The evolution of near wake structures in one cycle at $U^* = 10.91$, $C_\mu = 0.4019$, and $n = 1/2$.

cylinder, the process of combination with the vortex in the wake and shedding are observed (positions 4 and 5). Then, the jet is still strong enough to split another vortex in the shear layer at position 6 till the jet terminates at position 7. During the violent interaction between the jets and wake, the instability of the cylinder is highly excited by the energy obtained from the ambient flow. In addition, four more vortices shedding in the period of injection are dragged by the fast moving cylinder leaving a long wake in the transverse direction. Thus, the structures of the wake are markedly changed by the jet at large C_μ. Both RMS of C_y/C_{y0} and amplitude ratio are about 13 times the benchmarks. It can be concluded that the enhancements of the oscillation become violent as C_μ increases at $U^* = 10.91$.

As depicted in Fig. 8(c), different effects of n become more apparent compared with the cases at $U^* = 6.17$. When $n = 1/16$, the jet makes the vortex pattern transit from 2P to 2S and the oscillation is suppressed with amplitude decline by 67.8% as shown in Fig. 9(d). In addition, the oscillation frequency increases almost twice the benchmark. The detailed evolution of the near wake structures in a cycle for this suppressed case is illustrated in Fig. 11. It can be seen that the jet rushes out the shear layer to split the negative vortex and then disappear (positions 2–4) in the duration of $1/16T_3$. Under the influence of such momentary jet, the damping of the oscillator increases leading to the decrease in amplitude. So the control strategy with short duration and large C_μ will lead to high-frequency and low-amplitude oscillation that should be avoided. However, as n increases, more disturbances are injected into the flow field with more shedding vortices and larger travel in the transverse direction. At $n = 1/4$ and $1/2$, the amplitudes are elevated to about three times the benchmarks. Therefore, to stimulate the oscillation at a high reduced velocity, the jets with longer duration (1/4 and 1/2) are beneficial.

B. Effects on amplitude and frequency ratios

The amplitude ratio (A/D), an important parameter of the oscillation, is calculated by averaging 40 absolute values of the peaks after the flow field is fully developed. Meanwhile, the frequency ratio (f/f_n) is achieved by FFT (fast Fourier transform) of the displacements. The histories of A/D and f/f_n vs reduced velocity at different C_μ and n are shown in Figs. 12 and 13, respectively. In the figures, the histories with red squares represent the response of the smooth cylinder without control that is regarded as the benchmarks. According to the variation tendency of the amplitude ratios with control, the results can be divided into two distinct groups based on the reduced velocity: $U^* \leq 6.17$ and $U^* > 6.17$.

(a) When $U^* \leq 6.17$, the variation trends of amplitude ratios with control are almost in accordance with the smooth cylinder. As $C_\mu \leq 0.1005$, the amplitude ratios fluctuate around the benchmarks with quite small deviations (−19.6%–16.1%) for all n as shown in Figs. 12(a)–12(e). The tiny changes in amplitude ratios owe to the little disturbances into the flow field as mentioned in Sec. III A. As depicted in Figs. 12(f)–12(i), when $C_\mu > 0.1005$, the influences of different n on amplitude ratios become apparent where both suppression and stimulation occur. Due to the interaction between jet and

wake, the damping of the cylinder increases with a maximum drop of the amplitude ratio reaching 61.7% at $n = 1/16$. Energy absorption from the flow field is also observed with a maximum growth rate of 31.7% at $n = 1/2$. Though differences of amplitude ratios exist when $U^* \leq 6.17$ for different n, the deviations are relatively smaller than the cases at larger U^*. In addition, the frequency ratios are also very close to the benchmarks with the largest fluctuation of 10% at $n = 1/2$. Therefore, we can come to the conclusion that both n and C_μ have little effects on the amplitude and frequency responses within the initial branch ($U^* < 4.27$) and fore part of the upper branch ($4.27 < U^* \leq 6.17$).

(b) When $U^* > 6.17$, dramatic changes take place in the amplitude response. As $C_\mu < 0.1005$, all the controlled cases are higher than the benchmarks with a maximum increment of 334.3% that is much larger than the peak value (31.7%) at $U^* \leq 6.17$. Though high amplitude ratios are achieved, the deviations ($\leq 25.5\%$) between different n are still quite small. Combining with the cases at $U^* \leq 6.17$, it can be considered that the effects of different durations (n) at small momentum coefficients ($C_\mu < 0.1005$) are similar in the three branches. When $C_\mu \geq 0.1005$, the amplitude ratios increase with n and the deviations between different n enlarge at the same C_μ and U^*. Sudden jumps occur in the lower branch at $n = 1/2$ when $0.1005 \leq C_\mu \leq 0.2261$ where the oscillation mode shifts from VIV to galloping accompanied by the decrease in frequencies shown in Figs. 13(e)–13(g). The amplitude ratios increase approximately linearly vs U^* at $C_\mu = 0.3077$–0.4019 for $n = 1/2$ and $1/4$. Thanks to the occurrence of galloping phenomenon, the highest amplitude ratio reaches 3.31 that is 13 times the benchmark at $U^* = 10.91$. In the perspective of amplitude ratios, a higher value obtained in the lower branch means that a strong oscillation benefitting for energy harnessing is achieved. However, except for the enhancement, the amplitude ratio histories below the base lines are also observed at $n = 1/16$ for $C_\mu \geq 0.1570$ and $n = 1/8$ for $C_\mu \geq 0.3077$ where the oscillations are suppressed. Under the action of the jets, the damping of the cylinder is enlarged as mentioned in Sec. III A. At $U^* = 10.91$, $C_\mu = 0.4019$, and $n = 1/16$, the oscillation is almost totally suppressed with a tiny amplitude ratio and high frequency ratio, which means that the cylinder vibrates up and down violently with small displacements. Almost all the suppressed cases are at shorter n and larger C_μ. So it is necessary to avoid using the pulsed blowing jets with shorter durations and larger momentum coefficients to excite the oscillation of the cylinder.

C. Effects on energy harnessing

Apart from the near wake structures, hydrodynamic coefficients, amplitude ratios, and frequency ratios, power gain is another prominent index to measure the effects of the pulsed blowing jets on energy harnessing. As an active control method, the generation of the jets will consume some energy. Therefore, to assess the jets' effects on energy harnessing, the differences between the power done by forces exerted on the cylinder and consumed by the pulsed blowing jets are necessary to be calculated.

(1) The work (P) done by forces exerted on the cylinder in one cycle T_{osc} can be calculated as

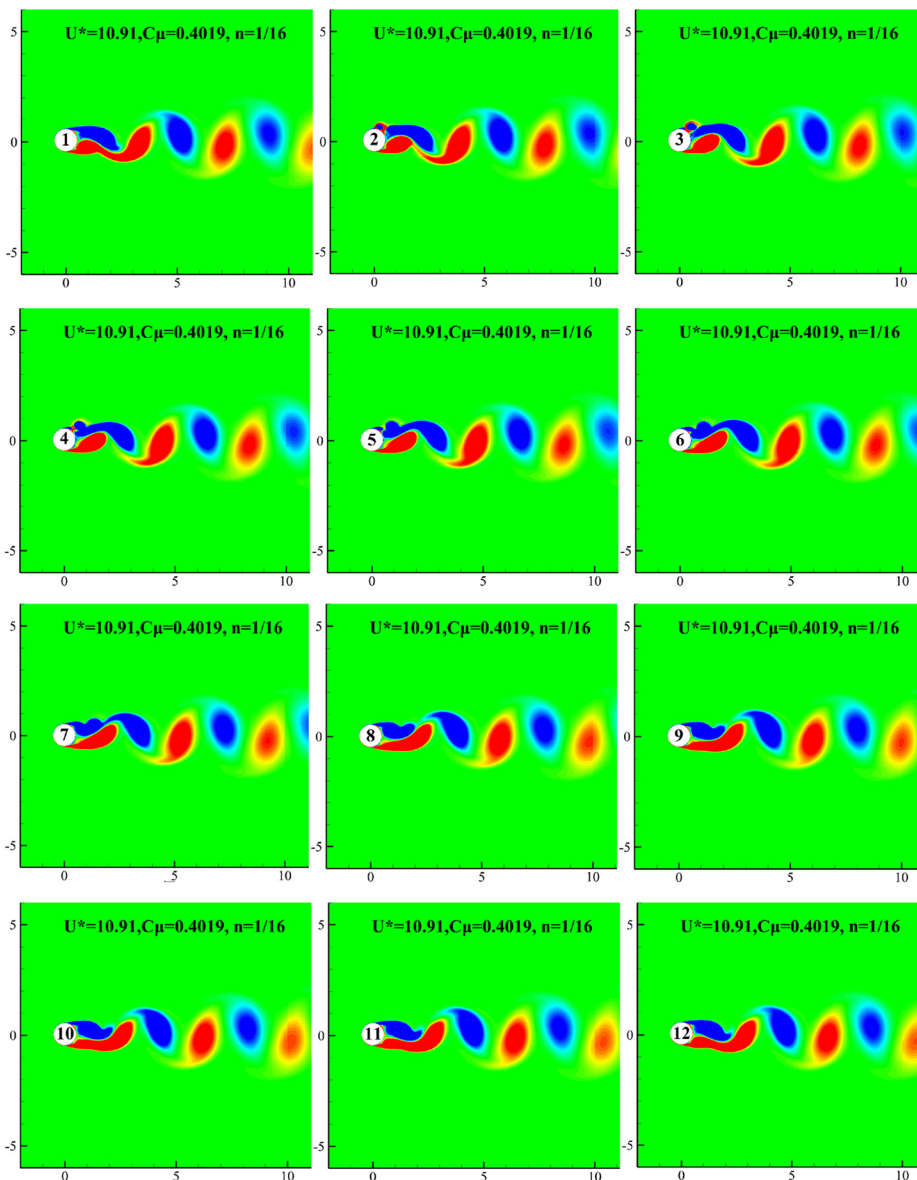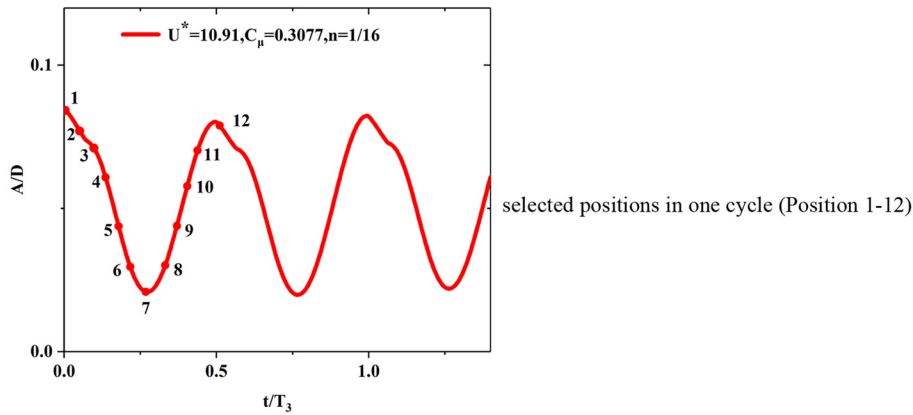selected positions in one cycle (Position 1-12)

FIG. 11. The evolution of near wake structures in one cycle at $U^* = 10.91$, $C_\mu = 0.4019$, and $n = 1/16$.
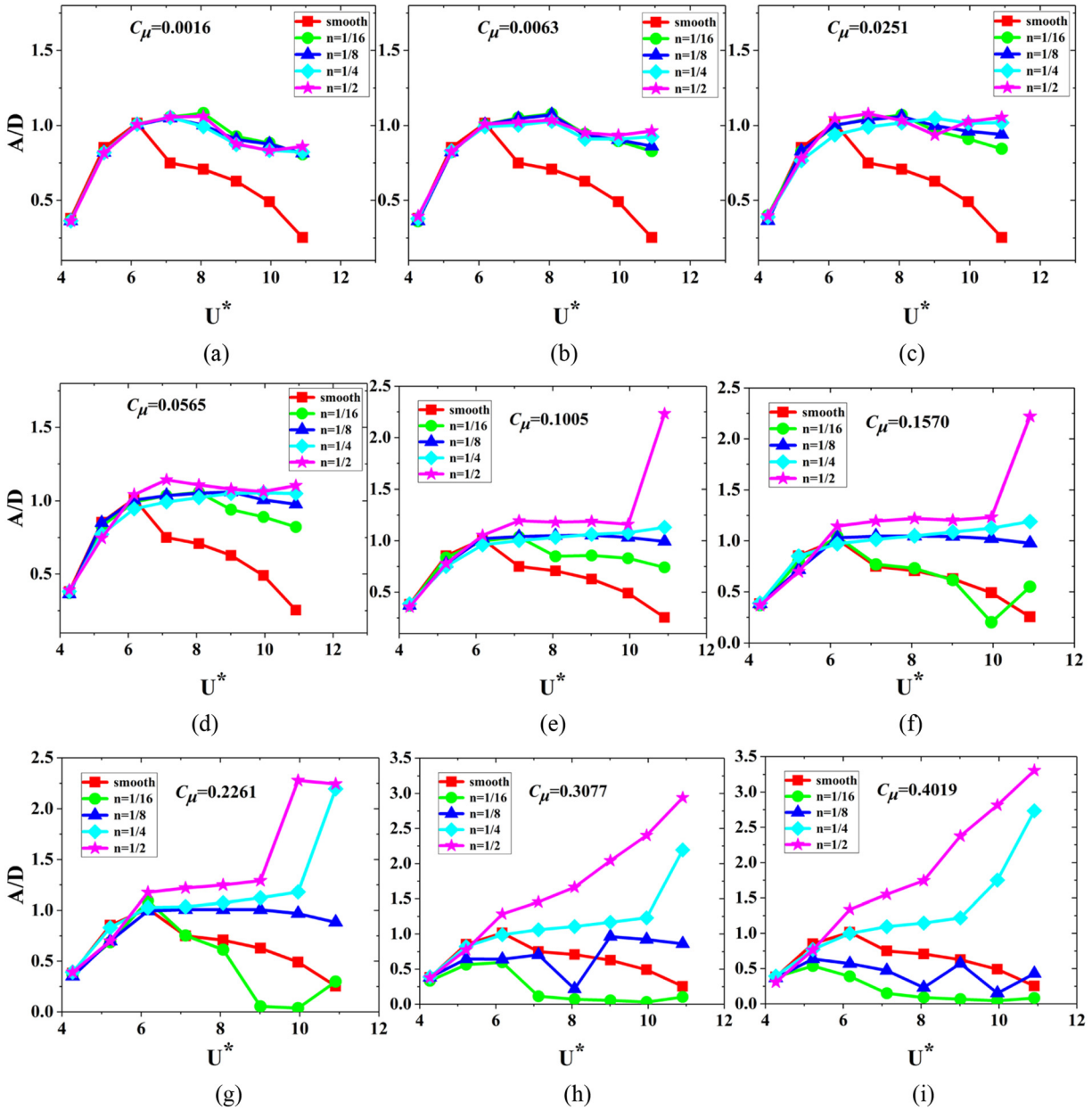
FIG. 12. Amplitude response vs reduced velocity at (a) $C_\mu = 0.0016$, (b) $C_\mu = 0.0063$, (c) $C_\mu = 0.0251$, (d) $C_\mu = 0.0565$, (e) $C_\mu = 0.1005$, (f) $C_\mu = 0.1570$, (g) $C_\mu = 0.2261$, (h) $C_\mu = 0.3077$, and (i) $C_\mu = 0.4019$ for various n.

$$P = \frac{1}{T_{OSC}} \int_0^{T_{OSC}} \left(F_{fluid,y,t} + F_{jet} \right) \cdot \dot{y} \cdot dt. \tag{18}$$

Substituting Eq. (8) in Eq. (18),

$$P = \frac{1}{T_{OSC}} \int_0^{T_{OSC}} \left(M \cdot \ddot{y} + c \cdot \dot{y} + k \cdot y \right) \cdot \dot{y} \cdot dt. \tag{19}$$

As the displacement of the cylinder is approximately sinusoidal,[39] the power can be simplified as

$$P = \frac{1}{T_{osc}} \int_0^{T_{osc}} c \cdot \dot{y}^2 dt. \tag{20}$$

The velocity ($\dot{y}$) of each time step in Eq. (20) has been calculated during the iterations in CFD. So the power ($P_{control}$ and P_{smooth}) done by the forces with and without control can be calculated in a cumulative way, respectively. So the changed power ΔP can be obtained as
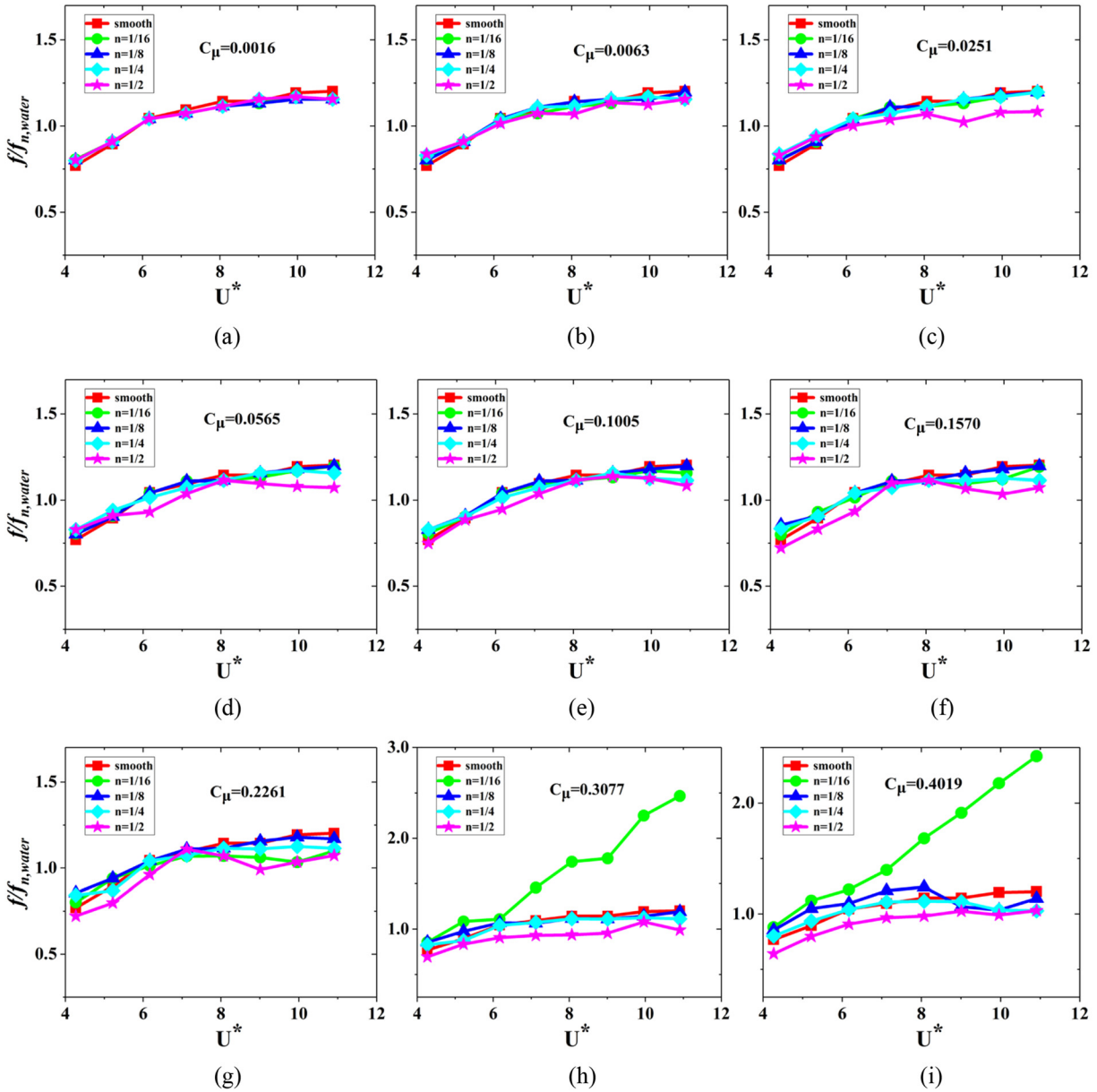
$$\Delta P = P_{control} - P_{smooth}. \tag{21}$$

FIG. 13. Frequency response vs reduced velocity at (a) $C_\mu = 0.0016$, (b) $C_\mu = 0.0063$, (c) $C_\mu = 0.0251$, (d) $C_\mu = 0.0565$, (e) $C_\mu = 0.1005$, (f) $C_\mu = 0.1570$, (g) $C_\mu = 0.2261$, (h) $C_\mu = 0.3077$, and (i) $C_\mu = 0.4019$ for various values of n.

(2) The power consumed by the pulsed blowing jets (P_{jet}) can be written as

$$P_{jet} = \frac{\frac{1}{2} \cdot \rho \cdot n T_{osc} U_{jet} \cdot w_{width} L \cdot U_{jet}^2}{T_{osc}} = \frac{\rho n w_{width} L}{2} \left(\frac{C_\mu U_\infty^2 D}{2d} \right)^{3/2}. \quad (22)$$

So the power gain P_{gain} is

$$P_{gain} = \Delta P - P_{jet}. \quad (23)$$

To get a dimensionless power gain, the power gain ratio η is introduced as

$$\eta = \frac{P_{gain}}{P_{fluid}} \times 100\%, \quad (24)$$

where the flow power P_{fluid}[39] is

$$P_{fluid} = \frac{1}{2} \rho U_\infty^3 DL. \quad (25)$$

If $\eta > 0$, the pulsed blowing jets are considered to be beneficial to enhance energy output; otherwise, control strategy is worthless. The

power gain ratios vs reduced velocity at different C_μ and n are shown in Fig. 14. In the figures, the red dashed lines denote $\eta = 0$. According to the variation trend, the results are divided into two parts based on the reduced velocity: $U^* \leq 6.17$ and $U^* > 6.17$.

(a) When $U^* \leq 6.17$, it can be seen that almost all the histories are close to or below the red dashed lines. In this range, as mentioned above, slight influences of the jets on the oscillation result in the values of power growth (ΔP) approaching 0. However, the necessary energy consumed by the pulsed blowing jets (P_{jet}) must be considered once the jets are on. So the minimally positive or negative power gain ratios are obtained inevitably without extra power to output. No matter what the values of C_μ and n are, the results show that the control in this range is worthless.

(b) When $U^* > 6.17$, the histories are all higher than zero lines at $C_\mu < 0.1005$ in Figs. 14(a)–14(d). In the range of $6.17 < U^* \leq 9.96$,

η increases first and then decreases with the reduced velocity, which are in accordance with the amplitude response with the values ranging from 5.45% to 19.78%. In addition, the deviations between the values of η for different n are quite small. Therefore, the outstanding performance to enhance energy harnessing with a relatively broad bandwidth is achieved when $U^* > 6.17$ and $C_\mu < 0.1005$.

When $0.1005 \leq C_\mu \leq 0.1570$, the power gain ratios η are smaller than the values at the same reduced velocity for $C_\mu < 0.1005$, due to the greater growth rate of P_{jet} than ΔP as C_μ increases, except for the cases at $U^* = 10.91$ as shown in Figs. 14(e) and 14(f). However, there are still high η ($\eta_{max} = 42.28\%$) at $U^* = 10.91$ where galloping occurs accompanied by large increment of ΔP. So a relatively narrower bandwidth for the enhancement is achieved for these two momentum coefficients. When $C_\mu > 0.1570$, although the amplitude
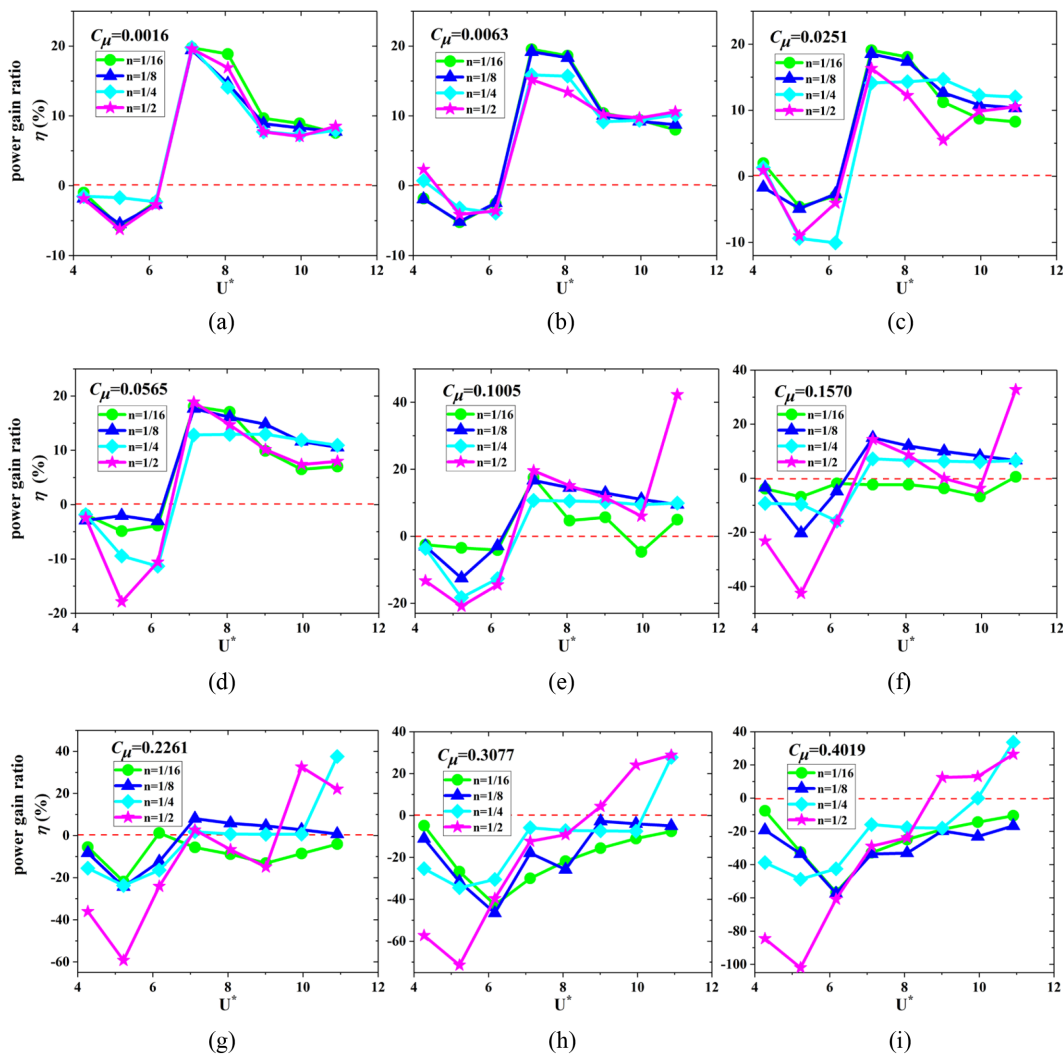

FIG. 14. Power gain ratios (η) vs reduced velocity at different C_μ and n: (a) $C_\mu = 0.0016$, (b) $C_\mu = 0.0063$, (c) $C_\mu = 0.0251$, (d) $C_\mu = 0.0565$, (e) $C_\mu = 0.1005$, (f) $C_\mu = 0.1570$, (g) $C_\mu = 0.2261$, (h) $C_\mu = 0.3077$, and (i) $C_\mu = 0.4019$.

ratios are quite large, P_{jet} is dominated in the power gain, and only a fraction of the cases is efficient ($\eta > 0$) for energy harnessing where the oscillation amplitude is extremely high as shown in Figs. 14(g)–14(i). Therefore, the jets falling in $U^* > 6.17$ and $C_\mu \geq 0.1005$ should be selected prudently to improve energy harnessing.

IV. CONCLUSIONS

After detailed comparisons of near wake structures, lift coefficients, amplitude ratios, frequency ratios, and power gain ratios, the major conclusions are summarized as follows:

(a) Based on the distribution of the wake structures, it can be seen that the interactions between jets and vortices in the near wake are distinct due to the variation of C_μ. The injected vortices at small C_μ ($C_\mu = 0.0016$) are trapped in the shear layer with a relatively small disturbance into the flow field. As C_μ increases, the injected vortices become strong enough to rush out of the shear layer, split the vortices, or even shed themselves and merge with other vortices during the downstream convection. As a result of the interaction, transitions of the vortex pattern and oscillation mode are observed in different branches. In the initial branch, no matter what the values of C_μ and n are, the vortex patterns keep 2S. The RMS of C_y/C_{y0} and amplitude ratios vibrate around the benchmarks within 10% and 20%, respectively. In the upper branch, different vortex patterns (2T and 2T + P_0) are observed and the amplitude ratios are slightly enhanced (31.7%) at large C_μ ($C_\mu \geq 0.1005$). In the lower branch, the oscillation of most cases are highly motivated, except for some suppressed cases at $C_\mu \geq 0.1570$, $n = 1/16$, and $1/8$. For the enhanced cases, the disturbances of the jets to wake become violent and more vortices shed in a cycle thanks to the energy absorption from flow field. Even galloping is observed at $C_\mu = 0.1005$–0.4019 and $n = 1/2$. However, at $C_\mu \geq 0.1570$ and $n = 1/16$ and $1/8$, the interactions increasing the cylinder's damping make the vortex patterns transit to 2S mode accompanied with the decline of amplitude ratios.

(b) Based on the amplitude and frequency responses, both the momentum coefficients (C_μ) and durations (n) have little effects on the oscillation in the initial branch and forepart of the upper branch ($U^* \leq 6.17$). As $U^* > 6.17$ and $C_\mu < 0.1005$, a maximum increment of 334.3% in amplitude ratio is achieved, but the small deviations between different n can be ignored. When $U^* > 6.17$ and $C_\mu \geq 0.1005$, the enhancement of the amplitude ratio is further improved at $n = 1/4$ and $1/2$, with the largest value about 13 times the benchmark. In addition, suppressed cases are observed at $n = 1/16$ and $1/8$ for $C_\mu \geq 0.1005$ that should be avoided.

(c) In the perspective of power gain, the effects of the jets are quite distinct. In the initial branch ($U^* \leq 6.17$), the power gain ratios are almost negative, which means that the control is worthless. However, in the range of $U^* > 6.17$ and $C_\mu < 0.1005$, the outstanding performance to enhance harnessing is achieved with the values of η ranging from 5.45% to 19.78%. As $U^* > 6.17$ and $C_\mu \geq 0.1005$, though the amplitudes reach high values, the efficient cases to improve energy

harnessing are quite few owing to the rapid growth of consumed energy by jets at large C_μ and reduced velocities.

The effects of various parameters, such as location of the micro-orifice, special position when jet is on, and types of the jets (synthetic jet or others), will be further researched in our future work.

AUTHOR DECLARATIONS
Conflict of Interest

The authors have no conflicts to disclose.

Author Contributions

Yujie Guo: Formal analysis (equal); Methodology (equal); Writing – original draft (equal). **Zhengui Huang:** Funding acquisition (equal); Project administration (equal); Resources (equal); Software (equal). **Chun Zheng:** Investigation (equal); Methodology (equal); Validation (equal). **Zhihua Chen:** Conceptualization (equal); Resources (equal); Supervision (equal); Writing – review & editing (equal).

DATA AVAILABILITY

The data that support the findings of this study are available within the article.

REFERENCES

[1] E. S. Kim et al., "Development of an alternating lift converter utilizing flow-induced oscillations to harness horizontal hydrokinetic energy," Renewable Sustainable Energy Rev. **145**, 111094 (2021).

[2] C. Wang and Y. Zhang, "Wave power extraction analysis for an oscillating water column device with various surging lip-walls," Ocean Eng. **220**, 108483 (2021).

[3] M. M. Bernitsas, "Harvesting energy by flow induced motions," in *Springer Handbook of Ocean Engineering* (Springer-Verlag, Berlin/Heidelberg, 2016), Chap. 47, pp. 1163–1244.

[4] C. Song et al., "Recent advances in ocean energy harvesting based on triboelectric nanogenerators," Sustainable Energy Technol. Assess. **53**, 102767 (2022).

[5] J. Wang et al., "The state-of-the-art review on energy harvesting from flow-induced vibrations," Appl. Energy **267**, 114902 (2020).

[6] E. Taheri et al., "Energy harvesting from inline vibration of an elastically mounted circular cylinder in oscillatory flow," Ocean Eng. **239**, 109694 (2021).

[7] R. D. Belvins, *Flow-Induced Vibration* (Krieger Publishing Company, Florida, 2001).

[8] B. Zhang et al., "Numerical investigation on effect of damping-ratio and mass-ratio on energy harnessing of a square cylinder in FIM," Energy **144**, 218–231 (2018).

[9] M. M. Bernitsas et al., "VIVACE (vortex induced vibration aquatic clean energy): A new concept in generation of clean and renewable energy from fluid flow," J. Offshore Mech. Arct. Eng.-Trans. ASME **130**, 041101 (2008).

[10] S. Barbarelli et al., "Preliminary performance assessment of a novel on-shore system recovering energy from tidal currents," Appl. Energy **224**, 717–730 (2018).

[11] H. Zhu, Y. Zhao, and T. Zhou, "CFD analysis of energy harvesting from flow induced vibration of a circular cylinder with an attached free-to-rotate pentagram impeller," Appl. Energy **212**, 304–321 (2018).

[12] X. Ma and S. Zhou, "A review of flow-induced vibration energy harvesters," Energy Convers. Manage. **254**, 115223 (2022).

10 July 2023 14:52:33

[13]Y. Lv et al., "A comprehensive review of nonlinear oscillators in hydrokinetic energy harnessing using flow-induced vibrations," Renewable Sustainable Energy Rev. **150**, 111388 (2021).

[14]G. Shi et al., "Hydrodynamic piezoelectric energy harvesting with topological strong vortex by forced separation," Int. J. Mech. Sci. **223**, 107261 (2022).

[15]L. Ding et al., "Flow induced motion and energy harvesting of bluff bodies with different cross sections," Energy Convers. Manage. **91**, 416–426 (2015).

[16]J. Wang et al., "Hybrid wind energy scavenging by coupling vortex-induced vibrations and galloping," Energy Convers. Manage. **213**, 112835 (2020).

[17]J. Wang et al., "On the use of metasurface for vortex-Induced vibration suppression or energy harvesting," Energy Convers. Manage. **235**, 113991 (2021).

[18]J. Wang et al., "Etching metasurfaces on bluff bodies for vortex-induced vibration energy harvesting," Int. J. Mech. Sci. **242**, 108016 (2023).

[19]W. Wu, M. M. Bernitsas, and K. Maki, "RANS simulation versus experiments of flow induced motion of circular cylinder with passive turbulence control at 35,000 < Re < 130,000," J. Offshore Mech. Arct. Eng.-Trans. ASME **136**, 041802 (2014).

[20]O. K. Kinaci et al., "Computational and experimental assessment of turbulence stimulation on flow induced motion of a circular cylinder," J. Offshore Mech. Arct. Eng.-Trans. ASME **138**, 041802 (2016).

[21]L. Ding et al., "Numerical simulation and experimental validation for energy harvesting of single-cylinder VIVACE converter with passive turbulence control," Renewable Energy **85**, 1246–1259 (2016).

[22]N. Li et al., "Hydrokinetic energy conversion using flow induced oscillations of single-cylinder with large passive turbulence control," Appl. Energy **308**, 118380 (2022).

[23]V. Tamimi, S. T. O. Naeeni, and M. Zeinoddini, "Flow induced vibrations of a sharp edge square cylinder in the wake of a circular cylinder," Appl. Ocean Res. **66**, 117–130 (2017).

[24]V. Tamimi et al., "Effects of upstream sharp edge square and diamond cylinders on the FIV of a circular cylinder," Mar. Struct. **59**, 237–250 (2018).

[25]V. Tamimi et al., "Marine hydrokinetic energy harvesting performance of diamond and square oscillators in tandem arrangements," Energy **202**, 117749 (2020).

[26]V. Tamimi et al., "Hydroelastic response and electromagnetic energy harvesting of square oscillators: Effects of free and fixed square wakes," Energy **263**, 125982 (2023).

[27]R. Tang et al., "Numerical analysis of WIV phenomenon with two in-series cylinders: WIV suppression and energy harvesting," Ocean Eng. **262**, 112154 (2022).

[28]R. Tang et al., "Hydrokinetic power scavenging from galloping phenomenon with two juxtaposed bluff bodies," Appl. Ocean Res. **121**, 103109 (2022).

[29]W. Ding et al., "Experimental and computational investigation of interactive flow induced oscillations of two tandem rough cylinders at $3 \times 10^4 \leq$ Re $\leq 1.2 \times 10^5$," Ocean Eng. **223**, 108641 (2021).

[30]B. S. Zhang et al., "Numerical investigation on VIV energy harvesting of bluff bodies with different cross sections in tandem arrangement," Energy **133**, 723–736 (2017).

[31]L. Ding et al., "Research on flow-induced vibration and energy harvesting of three circular cylinders with roughness strips in tandem," Energies **11**(11), 2977 (2018).

[32]W. Chen et al., "Review of active control of circular cylinder flow," Ocean Eng. **258**, 111840 (2022).

[33]H. Zhu et al., "Control of vortex-induced vibration of a circular cylinder using a pair of air jets at low Reynolds number," Phys. Fluids **31**(4), 043603 (2019).

[34]K. Zhou et al., "Sweeping jet control of flow around a circular cylinder," Exp. Therm. Fluid Sci. **141**, 110785 (2023).

[35]H. Jiang, "Separation angle for flow past a circular cylinder in the subcritical regime," Phys. Fluids **32**(1), 014106 (2020).

[36]R. Jackson, Z. Wang, and I. Gursul, "Control of upswept afterbody vortices using continuous and pulsed blowing," J. Aircr. **57**(1), 76–92 (2020).

[37]Y. Mei et al., "Active control for enhancing vortex induced vibration of a circular cylinder based on deep reinforcement learning," Phys. Fluids **33**(10), 103604 (2021).

[38]M. M. Zdravkovich, *Flow around Circular Cylinder: Fundamentals* (Oxford University Press, New York, 1997), Vol. 1.

[39]G. Zhao et al., "Numerical analysis of hydroenergy harvesting from vortex-induced vibrations of a cylinder with groove structures," Ocean Eng. **218**, 108219 (2020).

[40]F. A. C. Martins and J. P. J. Avila, "Three-dimensional CFD analysis of damping effects on vortex-induced vibrations of 2DOF elastically-mounted circular cylinders," Mar. Struct. **65**, 12–31 (2019).

[41]F. R. Menter, "Two-equation eddy-viscosity turbulence models for engineering applications," AIAA J. **32**(8), 1598–1605 (1994).

[42]H. Wang et al., "Control of two-degree-of-freedom vortex-induced vibrations of a circular cylinder using a pair of synthetic jets at low Reynolds number: Influence of position angle and momentum coefficient," Int. J. Heat Fluid Flow **80**, 108490 (2019).

[43]A. K. Soti and A. De, "Vortex-induced vibrations of a confined circular cylinder for efficient flow power extraction," Phys. Fluids **32**, 033603 (2020).

[44]X. Han et al., "Numerical simulation of super upper branch of a cylindrical structure with a low mass ratio," Ocean Eng. **168**, 108–120 (2018).

[45]M. Gu et al., "The effects of submergence depth on vortex-induced vibration (VIV) and energy harvesting of a circular cylinder," Renewable Energy **151**, 931–945 (2020).

[46]A. Khalak and C. H. K. Williamson, "Dynamics of a hydroelastic cylinder with very low mass and damping," J. Fluids Struct. **10**, 455–472 (1996).

[47]T. L. Morse and C. H. K. Williamson, "Prediction of vortex-induced vibration response by employing controlled motion," J. Fluid Mech. **634**, 5–39 (2009).

10 July 2023 14:52:33